JOURNAL OF GEOPHYSICAL RESEARCH, VOL. 106, NO. C10, PAGES 22,575–22,592, OCTOBER 15, 2001

Wave-formed sand ripples at Duck, North Carolina

Daniel M. Hanes, Vadim Alymov, and Yeon S. Chang
Department of Civil and Coastal Engineering, University of Florida, Gainesville, Florida, USA

Chris Jette
Seatek Inc., Gainesville, Florida, USA

Abstract. A recently developed acoustic multiple transducer array was utilized to measure small-scale bed forms in the nearshore and inner shelf regions at Duck, North Carolina. Two populations of wave-formed ripples were observed: short wave ripples (SWR) with heights ranging from 3 mm to 2 cm and lengths ranging from 4 to 25 cm and long wave ripples (LWR) with heights ranging from 3 mm to 6 cm and lengths ranging from 35 to 200 cm. The SWR were only present sometimes, and their presence or absence was determined by a critical value of the near-bed mobility number. The SWR were highly dynamic, sometimes flattening during wave groups and reforming over several incident wave periods. The LWR, in contrast, were almost always present. They were longer and lower relief than predicted by models or generally observed previously. Both SWR and LWR were often observed to migrate shoreward but were rarely observed to migrate seaward. The dimensions of the SWR, when they were present, were predictable by the *Nielsen* [1981] model or the *Wiberg and Harris* [1994] model to within approximately a factor of 2.

1. Introduction

Small-scale bed forms are intrinsic to the interactions between fluid and sediment near the seabed. For example, the fluid pressure distribution over a bed form causes a net resistance to the overlying flow. The hydraulic bed roughness, which is closely related to the bed form geometry, must therefore be prescribed in order to characterize the total flow resistance between the water and the seabed. Bed forms also have a profound effect upon the transport of suspended sediment because they affect the generation of turbulence and the entrainment of sediment near the seabed. So whether one's interests relate to hydrodynamics or sediment transport, bed form morphology is an important consideration.

Bed forms are found in extremely diverse aqueous and aeolian environments at the boundary between a moving fluid and a sedimentary bed. They exhibit a wide variety of shapes, patterns, and morphogeneses. In shallow coastal waters the dominant oscillatory motion of surface gravity waves often forms ripples on the seabed. These ripples typically have length scales ranging from a few centimeters to a few meters. They are sometimes irregular or have three-dimensional patterns, but are more commonly approximately two-dimensional. *Bagnold* [1946] reproduced two-dimensional ripples in the laboratory and under sufficiently energetic conditions, described the formation and ejection of a fluid vortex during each regular half cycle of oscillatory fluid motion. *Bagnold* [1946] called these ripples "vortex ripples" and suggested that the horizontal length scale of the ripples was determined by, and approximately equal to the fluid orbital diameter. Subsequent laboratory studies by *Carstens et al*. [1969], *Tunsdall and Inman* [1975], *Miller and Komar* [1980a], *Southard et al*. [1990], and *Mogridge et al*. [1994] have similarly emphasized two-dimensional vortex ripples caused by monochromatic oscillatory fluid motion. Field studies such as those by *Inman* [1957], *Dingler* [1974], *Dingler and Inman* [1976], *Miller and Komar* [1980b], *Boyd et al*. [1988], *Osborne and Vincent* [1993], *Vincent and Osborne* [1993], *Hay and Wilson* [1994], *Wheatcroft* [1994], *Thornton et al*. [1998], *Li and Amos* [1999], and *Traykovski et al*. [1999] have shown that while steady two-dimensional vortex ripples are sometimes found in nature, a variety of other types, patterns, and evolutions of bed forms are also possible. The variability in bed form morphology is consistent with the recognition that the hydrodynamic forcing is often a complex combination of currents and unsteady shoaled waves of many frequencies and directions, the sedimentary bed is composed of a combination of grains with different physical properties, and the hydrodynamic conditions are not necessarily in temporal equilibrium with the bed forms.

With respect to hydrodynamic conditions, for example, *Traykovski et al*. [1999] present observations of a transition from three- to two-dimensional ripples that are well correlated with an increase in the fluid orbital diameter near the seabed. During the intensifying portion of a storm the horizontal scales of both the three- and the two-dimensional ripples were observed to be approximately in equilibrium with the near-bed fluid orbital diameter. However, during the subsequent waning of the storm the two-dimensional ripple wavelengths remain unchanged for nearly one day despite a significant decrease in the near-bed fluid orbital diameter.

Although wave-formed bed forms have frequently been observed and reported upon by swimmers and divers, there has not been instrumentation available to make quantitative measurements, particularly measurements of heights, until recently. Most of the quantitative information about bed forms has been manually obtained by divers using mechanical devices. Such observations are generally limited to fair weather conditions in which divers can operate effectively and see suf-

Paper number 2000JC000337.
0148-0227/01/2000JC000337$09.00

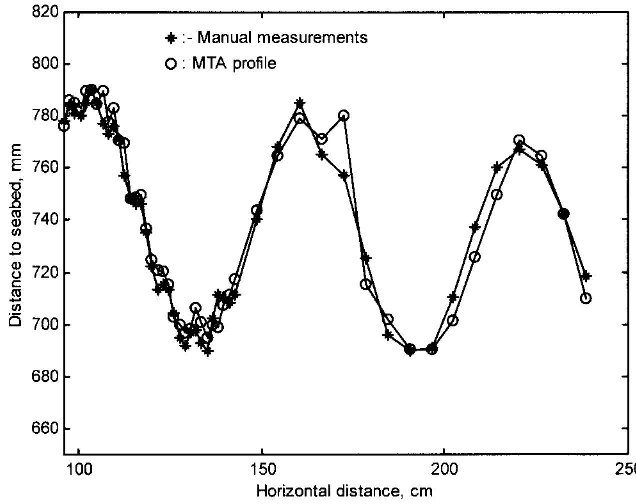

Figure 1. MTA and manual measurements of the location of a rippled sand bed.

ficiently far to observe the bed forms. Downward looking sonar systems have been mounted on a translating platform in order to make remote quantitative measurements of bed form height and length [e.g., *Dingler et al.*, 1977; *Greenwood et al.*, 1993], but these systems have been plagued by mechanical difficulties arising from the use of a moving platform underwater in the harsh nearshore environment. Side-scan and fan beam sonar devices have recently been utilized to measure bed form patterns and wavelengths [e.g., *Hay and Wilson*, 1994], but these systems do not provide accurate measurements of bed form height. Therefore, although there have been many observations of bed forms in the nearshore zone, most have been limited to fairly mild wave conditions. Furthermore, the observations of bed form height have generally not exhibited the accuracies consistent with modern instrumentation. For these reasons we were motivated to develop a new acoustic instrument capable of accurately measuring bed form height under both storm and fair weather conditions. This paper describes the new instrument, called a multiple transducer array (MTA), and the field observations obtained by the MTA in three different field deployments. We will first describe the capabilities of the MTA that was utilized to obtain the field measurements of bed forms. We will then describe the field techniques, provide an overview of our bed form observations, present some observations of bed form dynamics, compare the measured bed forms to model predictions, and, finally, provide a speculative discussion regarding the mechanisms responsible for the formation of the observed bed forms.

2. Multiple Transducer Array (MTA)

The MTA [see *Jette*, 1997; *Jette and Hanes*, 1998] is a linear array of sonar elements designed to accurately measure the dimensions of bed forms by measuring the distance from each transducer to the seabed. The MTA version that we most commonly used in the field was composed of three sections: a middle section of thirty-two 5-MHz transducers (hereinafter referred to as MTA1), each separated by 1.5 cm, and two side sections, each with sixteen 2-MHz transducers (hereinafter referred to as MTA2 and MTA3), each separated by 6 cm. When the MTAs are deployed ~50 cm above the bed, the 5-MHz transducers have an ~2-cm-diameter footprint on the seabed, and the 2-MHz transducers have an ~6-cm-diameter footprint. The transducer elements and their spacings were chosen such that the acoustic footprints on the seabed are approximately the same as the transducer separations so that aliasing is minimized. Each transducer is pinged in succession, and each acts as a threshold-detecting sonar device. A sweep of the entire 64 transducers takes ~2 s. An additional MTA (hereinafter referred to as MTA4) was also used to evaluate its accuracy in the laboratory. This unit consisted of thirty-two 5-MHz transducers, each separated by 2 cm.

The resolution of the MTA is determined by its ability to measure the elapsed time between the transmission of a sound pulse and the detection of the exceedance of a threshold return. This results in a resolution of ~1 mm. The accuracy of the MTA is more difficult to assess because it is influenced by a variety of environmental conditions as well as by the skill of the operator. We conducted a variety of tests in the laboratory in an attempt to quantify the accuracy of the MTA, as will be described below.

Three templates were constructed to enable the creation of sand beds ($D_{50} = 0.15$ mm) with shapes chosen to resemble idealized field observations. Template 1 has a smooth sloping bed with a slope of 1/20, template 2 has a horizontal bed with short-scale sinusoidal ripples, and template 3 has a horizontal bed with superimposed short- and long-scale sinusoidal ripples. In each case we first estimate the accuracy of the individual transducers and then estimate the accuracy of determining the ripple dimensions from the array. The transducer-measured distances to the seabed are compared to physical measurements obtained manually with a ruler. Examples of the MTA measurements and the manual measurements for template 3 are given in Figure 1.

Table 1 presents the root-mean-square (RMS) difference between MTA4 and the manual measurements. The accuracy of the MTA, as given by the RMS difference between the MTA estimates and the manual measurements, approaches the resolution of the MTA for the case of a flat, sloping bed and also for the case of short-scale ripples. The accuracy degrades to ~3 mm for the combination of long- and short-scale ripples because of the more extreme slopes that occur. An accuracy of 3 mm represents a significant improvement over previous methods of measuring ripples in the field through photographs, diver observations, and fan-beam or scanning sonars.

Estimating the ripple dimensions from the MTA measurements involves the sometimes complicated issue of defining a shape and estimating the shape and dimensions from a fixed array of measurement points. We have applied two different techniques to estimate the shape and dimensions of bed forms. Technique 1 identifies the zero upcrossings and extrema in the linearly detrended profile data to define individual ripples. Each pair of zero upcrossings or extrema provides an estimate of wavelength, and the difference in the successive extrema provides the height. This results in the estimation of a distri-

Table 1. RMS Difference Between MTA4 and Manual Measurements

Seabed Configuration	RMS Difference, cm
Smooth slope	0.14
Short ripples	0.13
Combined long and short ripples	0.27

Table 2. Measured and Estimated Ripple Dimensions

	Length, cm	Height, cm
Short ripple dimensions (known)	7	0.3
Technique 1 (estimated)	7	0.3
Technique 2 (estimated)	7.8	0.28
Long and short ripple dimensions (known)	60 and 6	9 and 1.0
Technique 1 (estimated)	61 and 6	8.9 and 1.0
Technique 2 (estimated)	58 and 7.0	8.2 and 0.83

bution of wavelengths and heights; the modal value of the histogram may then be chosen to provide one representative height and length. Technique 2 utilizes our prior knowledge of the ripple shape by fitting a sinusoidal shape to the measurements in a least squares sense, resulting in the estimation of a wavelength and amplitude for the sinusoid. For the case of combined long and short ripples the long-ripple dimensions are determined first. The long ripples are then detrended from the data, after which the short-ripple dimensions are estimated. The results are given in Table 2.

Interestingly, technique 1 is more accurate in estimating the ripple dimensions for both short-scale and combined short- and long-scale ripples. Technique 1 is also more appropriate for field observations because natural bed forms are not usually sinusoidal and they generally exhibit a distribution of lengths and heights. Therefore technique 1 was generally used to analyze field data, with the additional step described below.

The variability in the return from an individual transducer is greater in the field than in the laboratory primarily due to suspended sediment and, under some conditions, due to bed load sediment motion. Suspended sediment causes the scattering and loss of the transmitted sonar pulse. If the loss of acoustic energy is significant, then the return from the seabed may not exceed the set threshold and the estimated distance to the seabed will be incorrect. If the strength of the backscattered sound from a particular elevation above the bed is high because of the scattering of sound by suspended sediments, then that return may exceed the set threshold and its location will be misinterpreted as the location of the seabed, leading to an underestimation of the distance to the seabed. The scattering of sound by moving sediments is even more likely to occur if there is an active bed load sheet flow layer. Most models of sheet flow suggest that the thickness of the highly concentrated sheet is typically of the order of 10 grain diameters, which is usually less than the accuracy of the MTA. Fortunately, the disruption of accurate measurements due to the scattering of sound by moving sediment is generally short in duration. We have found it useful to make multiple measurements with each transducer and use the modal value in order to obtain accurate estimates of the seabed location. Under most field conditions that we have encountered, 15 scans were sufficient to obtain an accurate profile. The cost of such a sampling scheme is reduction of the temporal resolution of the MTA.

In our opinion the major strength of the MTA is obtaining accurate quantitative measurements of wave-formed ripples and local seabed slope under field conditions. The major weakness is that the profile is determined along a linear transect rather than over a two-dimensional region. Thus, in interpreting measurements obtained with an MTA we can address the cross-shore length scale of the ripples but not their three-dimensional character. Other instrumentation, such as a rotating, scanning sonar (RSS), can provide additional qualitative information about the three-dimensional patterns.

In the processing and interpretation of MTA data it is therefore necessary to assume the orientation of the bed forms in order to obtain cross-shore length measurements. *Traykovski et al.* [1999] and others have noted that the temporal evolution of ripple direction generally follows the dominant wave direction. Therefore our calculated lengths were multiplied by the correction factor cosine β, where β is the angle between the peak direction of the near-bed fluid motion and the orientation of the MTA. The typical correction factor for the data sets presented in section 3 was ~0.97, so this procedure turned out have a minimal effect on the data.

3. Field Observations

Bed form measurements were obtained in the nearshore zone at the U.S. Army Corps of Engineers Field Research Facility in Duck, North Carolina (Figure 2). Three different field experiments were carried out over a 3-year period. The first data set was recorded during August 23–25, 1995, and is referred to as the SIS95 data set. The second data set, referred to as SIS96, was recorded during October 29 to November 1, 1996. The Sensor Insertion System (SIS), a mobile crane-like device that permits rapid deployment of instruments from the research pier, was used to deploy the instruments in both of these experiments. The third data set was obtained from an array fixed in ~4-m water depth during the Sandyduck97 field experiment, held from September 11 to November 10, 1997. The Sandyduck97 data set is considerably more comprehensive than the SIS95 or SIS96 data sets and will receive the most emphasis here.

We utilized a suite of instruments designed for field investigations of small-scale sedimentation process observations in order to characterize the geometry and dynamics of wave-formed ripples. Hydrodynamics were measured with pressure sensors, electromagnetic current meters, and acoustic doppler velocimeters. A three-frequency acoustic backscatter sensor (ABS) measures suspended sediment concentration. An MTA and an RSS measure bed forms. An underwater video camera collects images of the seabed during periods of sufficient visibility, which were rare. All of the instruments are powered and controlled by a combination of microprocessor-based data loggers. Power is supplied from shore, and data are transmitted digitally to shore in real time for recording on a personal computer. The entire system is precisely synchronized to the microsecond, which is required for the ABS.

The SIS95 bedform data set was recorded using a prototype MTA that consisted of thirty-seven 5-MHz transducers with a center to center spacing of 1.2 cm, giving a total array length of 45 cm. Bed form profiles were recorded every 6 s during 30 data runs, each lasting 13 min. Measurements were made on the beach face, in the inner trough, near the inner bar, and offshore of the bar. Median sediment sizes ranged from 0.18 to 1.66 mm, water depths ranged from 1.6 to 6.8 m, and H_{m0} wave heights ranged from 0.2 to 0.9 m over the course of the experiment.

The SIS96 bed form measurements were made with a 64-element (three part) MTA described in section 2 and shown in Figure 3. Profiles were measured every 2 s. Thirty data runs were collected during SIS96; each ranged from 13 to 32 min in duration. The SIS96 measurements were also made at several cross-shore locations. Median sediment sizes ranged from 0.12

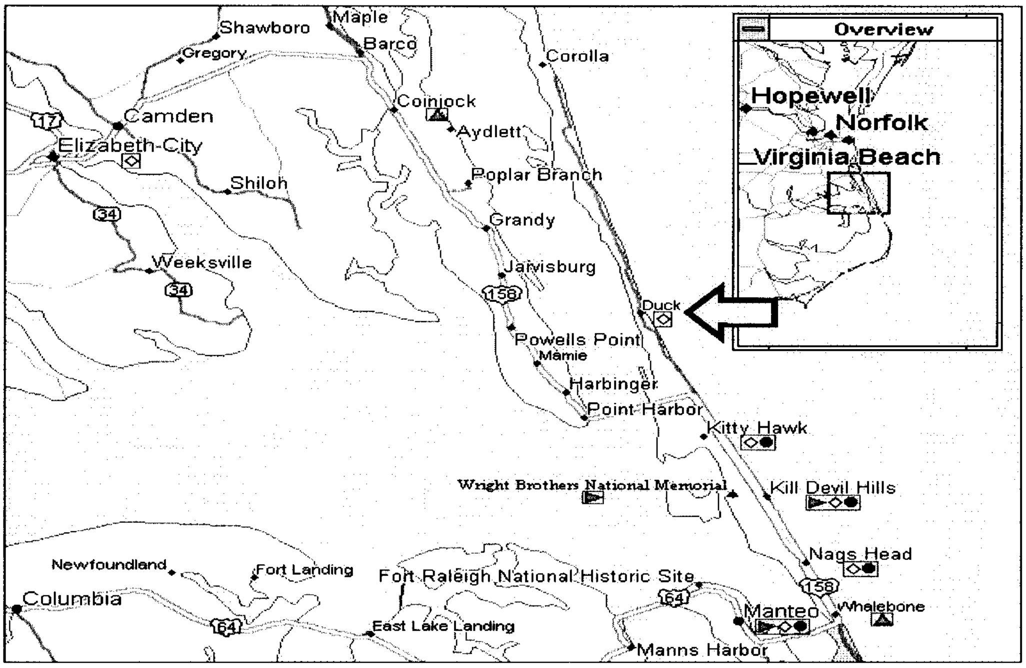

Figure 2. Location of the USACOE Field Research Facility.

to 0.21 mm, depths ranged from 1.4 to 7 m, and H_{m0} wave heights ranged from 0.32 to 1.2 m. The SIS96 experiment covered much more energetic flows than the SIS95 experiment.

The Sandyduck97 measurements were made with the same MTA as SIS96. Other instrumentation included a three-frequency acoustic backscatter system, two acoustic Doppler velocimeters, a pressure sensor, an optical backscatter sensor, an underwater video camera, and a rotating scanning sonar, as shown in Figure 3. MTA profiles were typically collected every 2 or 3 s for ~3 hours. Occasionally, this sampling scheme was varied during shorter or longer data collection periods. Approximately 300 hours of bed form data were collected during Sandyduck97 over a 2-month period.

4. Observed Ripple Dimensions

Bed forms are described and characterized most simply by their crest-to-trough height and their length between crests or troughs, analogous to the fundamental characteristics of a simple periodic curve such as a sinusoid. Such a description is only

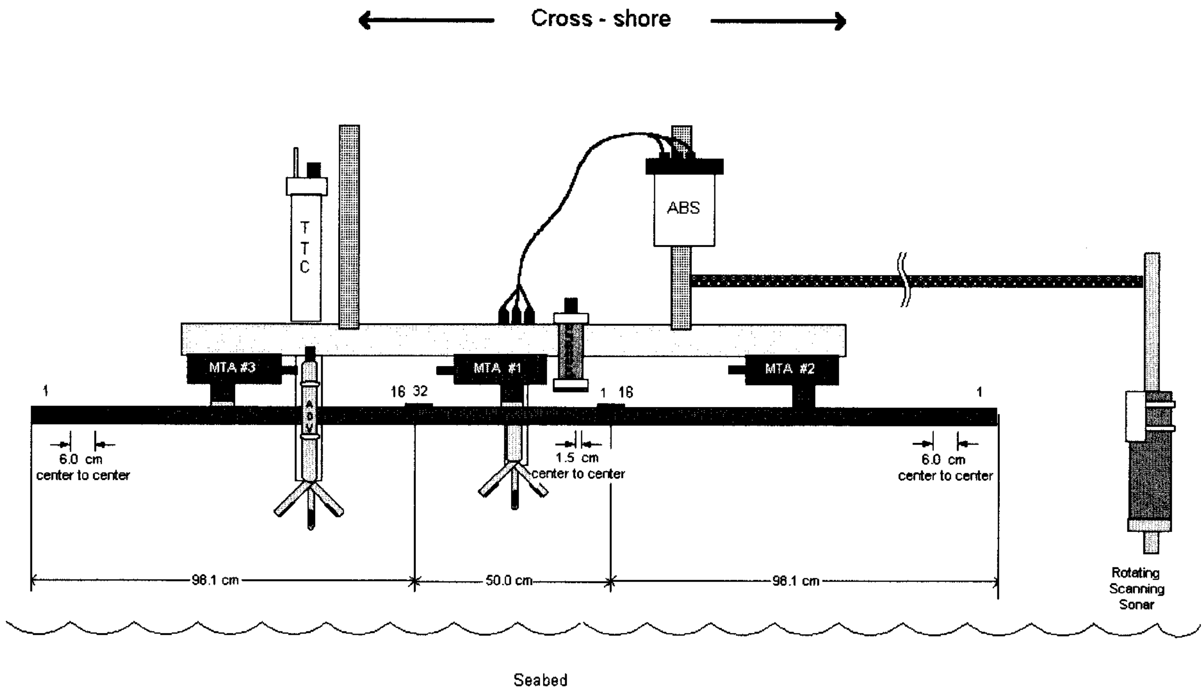

Figure 3. MTA array and other instruments as deployed in the Sandyduck97 experiment.

Table 3. Summary of Quality of Bed Form Observations

Run Description	MTA (1), SWR SIS95	MTA (1), SWR SIS96	MTA (1), SWR SD97	MTA (1, 2, and 3), LWR SIS96	MTA (1, 2, and 3), LWR SD97
Total runs	30	30	165	30	165
Excluded, possible aliasing	0	0	—	0	7
Excluded, poor quality	0	2	23	2	38
Good quality runs	30	28	142	28	120
Only SWR	30	10	5	—	—
Only LWR	—	—	—	5	93
Both SWR and LWR	—	—	—	13	18
No SWR or LWR (flat bed)	0	—	—	0	3

strictly accurate for two-dimensional bed forms with similar shapes. Real bed forms exhibit a wide variety of shapes and patterns that in some cases cannot be completely described by height and length alone. Nonetheless, it is useful to describe bed forms by their characteristic dimensions, particularly in applications that require the parameterized effects of the bed forms on the overlying fluid flow. In the idealized situation of simple harmonic flow over a uniform-sized sand bed the following parameters contain the significant length scales and timescales: The sediment is described by its characteristic size (typically diameter D) and density (ρ_s), and the fluid motion is described by the fluid orbital diameter (d_o) or fluid orbital semiexcursion ($A = 0.5d_o$) and by the fluid orbital period (T) or frequency (ω). Fluid material properties such as dynamic viscosity (ν) and density (ρ) are also important under some conditions, but these values vary only slightly for water under typical coastal conditions. Furthermore, in most applications, fluid momentum is transferred primarily by turbulence rather than by molecular diffusion, so the effects of fluid molecular viscosity variations are probably not generally significant to bed forms. Several dimensionless groups that relate to sediment transport and bed form morphology are typically formed from these parameters: (1) grain Reynolds number, $Re_g = A\omega D/\nu$; (2) orbital Reynolds number, $Re = A^2\omega/\nu$; (3) mobility number, $\psi = (A\omega)^2/[(S-1)gD]$, where S is the specific gravity (ρ_s/ρ); (4) Shields parameter, $\theta = 0.5f_w\psi$, where f_w is the skin friction factor; and (5) period parameter, $D/(S-1)gT^2$. The vertical length scale, again for idealized harmonic fluid motion, can be estimated by the displacement thickness of the boundary layer, δ_d, and is mainly determined by the fluid orbital semiexcursion, $\delta_d = 0.5f_wA$ [e.g., see *Nielsen*, 1992], or by the fluid orbital diameter, $\delta_d \approx 0.04d_o$ [see *Wiberg and Harris*, 1994]. For these reasons the dimensions of wave-formed ripples are often normalized by the fluid orbital diameter.

In the coastal environment the hydrodynamic quantities are essentially random because of the temporal variations in wave direction and amplitude. In this case the orbital diameter and mobility number are typically calculated using representative values for the wave height and period estimated from the surface elevation spectrum and from linear wave theory. According to linear wave theory, $d_o = H_{m0}gk/(\omega_{\text{peak}}^2 \cosh kh)$, where H_{m0} is the wave height estimated from the surface elevation spectrum, g is acceleration due to gravity, k is wave number, h is local depth, and $\omega_{\text{peak}} = 2\pi/T_{\text{peak}}$ is peak wave radian frequency. In section 7 we will also make use of the significant near-bed fluid orbital diameter, $d_{o,1/3}$ ($= 2A_{1/3}$), as defined by the following technique. The measured time series of cross-shore velocity was transformed using linear wave theory to estimate the velocity near the seabed. Then the time series of water particle excursion was calculated as the time integral of the velocity time series. To get the significant near-bed orbital diameter $d_{o,1/3}$, all zero upcrossings were found, and the maximum and minimum excursions from the mean were obtained between each upcrossing. The difference between the maximum and minimum was recorded as near-bed orbital diameter. The significant near-bed orbital diameter was calculated as the average of the highest one third of these orbital diameters. The significant near-bed mobility number ψ_s is defined as $\psi_s = (A_{1/3}\omega_{pb})^2/[(S-1)gD]$. In this expression, ω_{pb} is the peak radian frequency ($2\pi/T_{pb}$) determined from the near-bed orbital excursion spectrum. The peak frequency or period near the seabed may be different than the peak frequency of the surface elevation because of the frequency-dependent reduction of fluid orbital amplitude with depth.

Table 3 summarizes the quality and quantity of bed form measurements obtained during the three experiments. In principle, an MTA can measure ripples with lengths ranging from twice the transducer separation up to the entire array length. The central MTA(1) was therefore capable of measuring ripples with length scales ranging from 3 to 45 cm and the side MTAs (2 and 3) were capable of measuring ripples with length scales ranging from 12 to 240 cm. Certain runs were excluded because the raw data were extremely noisy. These are indicated in Table 3 as poor quality because after the procedure of removing minor noise due to false returns of the MTA, there still were significant spikes remaining that affected the proper calculation of ripple dimensions. Seven out of 165 runs were also excluded from the Sandyduck97 data set because of the possibility that short wave ripples were aliased into apparent long wave ripples. Although the transducer spacing and characteristics were chosen to minimize this possibility, we decided to exclude the few runs where the long-scale ripples were equal to or lower than the short-scale ripples in height to eliminate any possibility of aliasing. A summary of the hydrodynamics and bed form dimensions for the SIS95, SIS96, and Sandyduck97 experiments are given in Tables 4, 5, and 6, respectively.

We generally observed bed forms with two different ranges of wavelength: shorter ripples with wavelengths of ~5–25 cm and long ripples with wavelengths of ~35–240 cm. The identification of two scales of bed form lengths is consistent with the observations of *Osborne and Vincent* [1993] that were obtained at a macrotidal beach in SW England. We will refer to the two populations of ripples as short wave ripples (SWR) and long wave ripples (LWR). Specific examples of measured ripple profiles and histograms of their dimensions are shown in

Table 4. Hydrodynamics and Ripple Dimensions For SIS95 Experiment, August 23–August 25, 1995[a]

Run	Depth, m	H_{m0}, m	T_{peak} Sea Surface, s	T_{peak} Seabed, s	D_{50}, mm	Sign. Orb. Dia., cm	Orbital Dia., cm	SWR Length, cm	SWR Height, cm
1	6.1	0.71	3.8	16.0	0.285	50	23	13	1.6
2	6.33	0.65	3.8	16.0	0.285	52	20	10	1.4
3	6.42	0.8	4.3	16.0	0.285	50	36	13	1.5
4	6.53	0.66	4.3	16.0	0.285	58	29	14	1.8
5	6.58	0.73	4.3	16.0	0.285	47	31	15	1.8
6	6.69	0.83	4.3	16.0	0.285	59	35	14	1.6
7	6.78	0.85	4.6	16.0	0.285	55	42	14	1.5
8	6.79	0.92	4.9	16.0	0.285	62	54	14	1.4
9	6.82	0.85	4.3	16.0	0.285	56	35	14	1.5
10	6.16	0.41	4.9	16.0	0.285	50	27	10	1.4
11	1.94	0.31	4.3	16.0	0.176	86	41	13	1.1
12	1.9	0.31	4.6	16.0	0.176	69	45	13	1.2
13	1.62	0.27	4.6	16.0	0.176	69	43	12	1.3
14	1.65	0.38	6.4	7.1	0.238	100	89	12	1
15	1.63	0.21	4.3	16.0	0.207	55	31	13	1.2
16	1.76	0.22	4.6	16.0	0.207	59	33	11	1.4
17	1.82	0.23	4.6	16.0	0.207	57	34	10	1.2
18	1.91	0.24	4.3	16.0	0.207	65	32	12	0.9
19	1.99	0.26	16.0	16.0	0.207	67	146	8	0.8
20	2.14	0.25	5.3	16.0	0.207	62	41	7	0.8
21	2.25	0.27	7.1	16.0	0.207	65	60	9	0.9
22	4.19	0.37	7.1	12.8	0.397	65	57	18	3
23	4.21	0.31	7.1	16.0	0.397	54	48	16	2.6
24	3.9	0.44	6.4	16.0	0.641	90	62	10	1.9
25	3.86	0.63	8.0	12.8	1.124	126	117	13	2
26	3.8	0.69	7.1	7.1	1.124	121	113	13	2
27	2.8	0.28	7.1	16.0	1.662	54	55	12	1.5
28	2.72	0.29	7.1	16.0	0.175	59	58	21	1.5
29	2.25	0.22	7.1	7.1	1.466	53	49	16	2.5
30	2.2	0.24	6.4	12.8	1.466	56	48	17	2.4

[a]Run, numerical sequence of runs during experiment; Depth, time-averaged water depth at instruments during run; H_{m0}, significant wave height calculated using spectral method; T_{peak} Sea Surface, peak period from sea surface elevation spectrum; T_{peak} Seabed, peak period from spectrum of near-bed orbital excursion; D_{50}, median sand grain diameter from sieve; Significant Orbital Diameter average of the highest one third of the near-bed orbital diameters; Orbital Dia., near-bed orbital diameter from H_{m0} and T_{peak} using linear wave theory; SWR Length, small wave ripple length from peak in the histogram of ripple lengths; SWR Height, small wave ripple height from peak in histogram of ripple heights.

Figures 4 (SWR) and 5 (LWR), where each grid represents ~3 hours of measurements. Upon occasion, the SWR were superimposed upon the LWR, but under most conditions either the SWR or LWR were mainly present. The examples shown in Figures 4 and 5 were chosen to illustrate the complexity in interpreting this data set. For example, although the seabed maintains its basic shape over each of these 3-hour measurement periods, the vertical location of the seabed at each horizontal location varies by ~0.5–1.0 cm. It is also apparent that the ripples are not uniform and periodic; they exhibit a variety of length scales. For these reasons we have used statistical approaches to describe the measurements.

Our measurements of bed form dimensions can be summarized by their probability density functions, as shown in Figures 6 and 7 for SWR and LWR, respectively. We have divided these probability density functions into the two subsets of ripples (SWR and LWR) because they appear to be two separate distributions (as will be shown more clearly below). Each observation has been weighted by the bed form length and the duration of the observation in the construction of these overall distributions so that the total area under each distribution is equal to one. The weighting by length is required because the number of ripples measured by the fixed-length arrays is inversely proportional to their length if the ripples are periodic.

The SWR heights range from ~0.3 to 2 cm, and the lengths range from 4 to ~25 cm. The SWR length distribution is relatively unimodal, with a peak near 8 cm, and the height/length ratio peaks near 0.07. A length of 8 cm for the Sandyduck97 observations corresponds to a length/sediment diameter ratio of ~540, which corresponds well with the *Clifton* [1976] or *Wiberg and Harris* [1994] description of anorbital ripples. The LWR length distribution, in contrast to the SWR distribution, is irregular and multimodal. LWR lengths range from 35 to ~200 cm, and their heights vary from 0.3 to ~6 cm. The modal value of the height-to-length ratio, or steepness, is ~0.01. These ripples have relatively low relief when compared to classical vortex ripples that have typical steepness of ~0.15. While there are many previous observations of bed forms with the length scales of our LWR, the only previous measurements of similar low steepness ripples that we are aware of was recently reported by *Vincent et al*. [1999]. We can speculate that both SWR and LWR with heights <0.3 cm were probably sometimes present, but these periods were classified in Table 3 as flat beds because the ripple height was less than the accuracy of the MTA.

Our measurements of bed form height and length are presented and compared to previously published field measurements [*Nielsen*, 1981; *Inman*, 1957; *Dingler*, 1974] of bed form dimensions as a function of the significant near-bed fluid orbital diameter (Figure 8). There are large variations in the data (note the log scales), but the ripple lengths clearly cluster into two different groups, as noted earlier. There is a sparsely populated gap in the ripple lengths between ~20 and 40 cm. The lines in Figure 8a are shown simply to aid in visualizing the

Table 5. Hydrodynamics For SIS96 Experiment, October 29 Through November 1, 1996[a]

Run	Depth, m	H_{m0}, m	T_{peak}, Sea Surface, s	T_{peak} Seabed, s	D_{50}, mm	Orbital Direction, deg	Sign. Orb. Dia., cm	Orbital Dia., cm	SWR Length, cm	SWR Height, cm	LWR Length, cm	LWR Height, cm
1	5.8	1.21	6.4	6.4	0.121	2	97	121	7	0.4	plane	plane
2	5.7	0.99	6.4	6.4	0.121	−8	98	115	7	0.3	plane	plane
3	5.7	0.9	6.4	6.4	0.121	4	87	97	8	0.5	plane	plane
4	5.7	0.61	5.82	12.8	0.121	16	72	55	7	0.6	plane	plane
5	3.9	0.48	10.67	12.8	0.19	0	96	108	11	1.2	2.7	82
7	3.1	0.52	10.67	12.8	0.196	−14	121	181	17	1.5	3.5	73
8	2.9	0.4	4	12.8	0.202	−20	77	40	13	1.3	plane	plane
9	1.6	0.32	9.85	16.0	0.185	0	183	222	plane	plane	5.6	123
10	1.4	0.32	9.85	12.8	0.185	−2	212	142	plane	plane	2.8	160
11	1.4	0.59	12.8	12.8	0.208	−10	201	320	plane	plane	2.7	158
12	2.4	0.36	7.11	10.7	0.184	−6	112	116	20	2	plane	plane
13	2.5	0.39	10.67	10.7	0.186	−4	116	102	12	0.9	plane	plane
14	2.7	0.6	10.67	10.7	0.208	−4	187	188	8	0.4	2.8	247
15	2.6	0.55	10.67	10.7	0.208	−8	178	167	7	0.3	3.0	250
16	2.5	0.55	10.67	10.7	0.208	−10	178	166	7	0.3	3.2	248
17	2.5	0.48	8	10.7	0.208	−14	150	134	8	0.4	3.2	249
18	2.4	0.51	9.85	10.7	0.208	−6	169	172	9	0.3	3.1	246
19	2.8	0.55	10.67	10.7	0.202	−6	162	163	plane	plane	7	122
20	2.6	0.69	10.67	10.7	0.202	−2	227	209	10	0.3	6.7	127
21	2.6	0.59	10.67	10.7	0.202	−10	177	166	5	0.6	6	108
22	2.9	0.54	9.14	10.7	0.192	−6	196	182	6	0.2	12.6	185
23	3.1	0.55	11.64	11.6	0.192	−4	166	175	8	0.3	11.1	157
25	3.2	0.37	11.64	11.6	0.18	−6	102	127	14	1.3	plane	plane
26	3.7	0.48	10.67	10.7	0.19	−2	135	122	14	1.1	6.2	149
27	3.6	0.47	10.67	10.7	0.19	−2	123	131	17	1.4	6.4	161
28	7	0.46	10.67	10.7	0.121	−4	95	91	7	0.5	plane	plane
29	7	1.11	3.12	11.6	0.121	−6	79	19	7	0.6	plane	plane
30	2.8	0.48	10.67	10.7	0.179	−2	151	142	plane	plane	7.6	151

[a]Run, numerical sequence of runs during experiment; Depth, time-averaged water depth at instruments during run; H_{m0}, significant wave height calculated using spectral method; T_{peak} Sea Surface, peak period from sea surface elevation spectrum; T_{peak} Seabed, peak period from spectrum of near-bed orbital excursion; D_{50}, median sand grain diameter from sieve; Orbital Direction, peak direction of near-bed orbital motion in degrees north of shore normal; Sign. Orb. Dia., average of the highest one third of the near-bed orbital diameters; Orbital Dia., near-bed orbital diameter from H_{m0} and T_{peak} using linear wave theory; SWR Length, small wave ripple length from peak in the histogram of ripple lengths; SWR Height, small wave ripple height from peak in histogram of ripple heights; LWR Length, large wave ripple length from peak in histogram of ripple lengths; LWR Height, large wave ripple height from peak in histogram of ripple heights; plane, no ripples >3 mm detected using histogram technique; aliased, SWR might have aliased LWR estimates.

two families of ripple lengths. Ripple heights, in contrast, show no obvious patterns or groupings related to wave orbital diameter. The heights of SWR and LWR overlap without any clear separation. Note that although SWR and LWR are both present over a large range of orbital diameters, there are no SWR (lower cluster of points) for orbital diameters greater than ~2–3 m. The disappearance of SWR under intense hydrodynamic conditions is well known and will be discussed further in section 5. There are also no LWR for orbital diameters less than ~60 cm, but this may be because during the Sandyduck97 experiment the orbital diameter was rarely <60 cm.

The influence of the hydrodynamics upon the ripple dimensions can be examined further by plotting them as a function of the significant near-bed mobility number. Figure 9 shows the results for our three data sets. The variability in the measurements is perhaps the most striking feature of this presentation. It will not be surprising to find in section 7 that predictive models for ripple height and length have a high degree of error.

5. SWR Flattening and Reformation

It is interesting that SWR were only sometimes present but LWR were nearly always present during the Sandyduck97 experiment. Table 3 shows that SWR were present during ~22% of the good quality runs during Sandyduck97. In contrast, LWR were present during ~93% of the good quality runs at the same location during the same overall period. *Dingler* [1974] proposed and *Nielsen* [1981] verified that if mobility number exceeds 240, then vortex ripples are wiped out and the seabed becomes flat. In the context of our measurements we would interpret this as the disappearance of SWR at high mobility numbers. We have examined the mobility number for a possible threshold for the presence or absence of SWR for the SIS96 and Sandyduck97 data, as shown in Figure 10. SWR were present 85% of the time when the mobility number was <65, but SWR were only present 13% of the time when the mobility number was >65. No SWR were observed when the mobility number was >185. In contrast, LWR were present over a wide variety of the mobility numbers, as is shown in Figure 10c. The reason that the number of LWR present at low mobility numbers is greater than the number of LWR present at high mobility numbers is that the latter conditions happen less often.

It appears that the SWR occur within a range of mobility numbers that are large enough to move sediment but not so large as to cause flattening. This tendency for SWR to flatten under large waves can also be seen in time series measure-

Table 6. Hydrodynamics During Sandyduck97 Experiment, September 11 Through November 10, 1997[a]

Run	Depth, m	H_{m0}, m	T_{peak}, Sea Surface, s	T_{peak} Seabed, s	D_{50}, mm	Orbital Dir., deg	Sign. Orb. Dia., cm	Orbital Dia., cm	SWR Length, cm	SWR Height, cm	LWR Length, cm	LWR Height, cm
1	3.94	1.16	6.4	12.8	0.157	8	283	162	plane	plane	140	1.2
2	3.59	1.54	10.7	12.8	0.157	14	350	416	plane	plane	130	1.2
3	4.57	1.37	11.6	12.8	0.157	12	288	354	plane	plane	134	1
4	3.58	0.83	10.7	12.8	0.157	14	223	225	plane	plane	76	0.6
5	4.6	1.05	11.6	10.7	0.157	14	189	269	plane	plane	72	0.6
6	3.61	0.75	9.8	11.6	0.157	14	195	185	plane	plane	83	0.8
7	4.58	0.65	9.8	9.8	0.157	14	167	139	plane	plane	83	1
8	3.65	0.69	10.4	11.6	0.157	18	223	180	plane	plane	202	1.7
9	3.57	0.72	10.7	12.8	0.157	16	190	199	plane	plane	270	1.1
10	4.67	0.82	11.1	11.1	0.157	14	221	196	plane	plane	154	1.4
11	4.46	0.63	10.4	12.8	0.157	14	152	147	plane	plane	162	1.4
12	3.38	0.59	11.6	11.6	0.157	18	159	180	plane	plane	151	1.4
13	4.76	0.42	9	11.6	0.157	14	100	79	21	1	55	2
14	3.34	0.52	10.7	12.8	0.157	16	103	145	11	0.8	73	1.8
15	4.55	0.32	10.9	19.7	0.157	14	94	76	13	0.8	82	2.5
16	3.83	0.49	11.6	19.7	0.157	20	112	138	12	1.4	73	2.4
17	4.76	0.35	10.7	19.7	0.157	10	78	79	12	1.3	69	2.2
18	3.87	0.31	13.5	13.5	0.157	10	88	104	9	0.6	35	1
19	4.33	2	6.8	7.8	0.157	52	393	287				
20	5.03	1.61	6.7	8.0	0.157	44	227	206				
21	3.85	1.23	7.8	8.0	0.157	42	212	221	plane	plane	plane	plane
22	4.6	1.07	7.5	8.0	0.157	26	131	167	plane	plane	226	3.2
23	4.53	0.76	8.3	8.0	0.157	24	134	134	plane	plane	228	3.3
24	4.27	0.63	13.5	12.8	0.157	12	141	202	plane	plane	208	3.1
25	4.23	0.54	8.8	13.5	0.157	14	132	107	plane	plane	231	3.6
26	3.62	0.56	13.5	13.5	0.157	12	154	195	plane	plane	200	3.5
27	3.83	1.37	5.7	12.8	0.157	44	172	167	plane	plane	plane	plane
28	4.49	0.88	6.2	9.1	0.157	40	136	109	plane	plane	184	2.2
29	3.75	0.77	7.1	8.5	0.157	20	145	127	plane	plane	231	4.3
30	4.17	0.99	6.2	7.5	0.157	12	155	128	plane	plane	247	5.3
31	4.48	0.86	7.1	7.1	0.157	14	131	126	plane	plane	250	4.7
32	3.86	0.57	8	8.0	0.157	16	128	105	plane	plane	239	5.6
33	3.93	0.37	10.2	8.5	0.157	12	99	91	6	0.8	120	4
34	3.84	0.34	6.2	9.1	0.157	6	87	47	25	1.1	104	2.8
35	4.47	0.44	8.3	8.5	0.157	4	82	79	16	1.2	102	3.3
36	4.21	0.47	6.7	8.5	0.157	16	93	68	7	0.6	127	4
37	4.13	0.65	8.8	9.1	0.157	16	115	130	plane	plane	127	2.7
38	3.8	1.05	4.1	8.5	0.157	18	144	75	plane	plane	151	4
39	4.56	1.37	4.7	8.5	0.157	18	127	110	plane	plane	101	5.4
40	4.39	1.1	4.5	8.5	0.157	6	205	83	plane	plane	117	1.2
41	4.32	1.48	7.3	7.1	0.157	10	236	230	plane	plane	65	0.6
42	3.68	0.99	6.6	7.5	0.157	8	234	150	plane	plane	60	0.5
43	4.37	0.88	7.1	7.1	0.157	4	193	132	plane	plane	249	1.6
44	4.25	0.95	6.9	9.1	0.157	10	195	140	plane	plane	245	2.6
45	4.29	0.47	7.5	8.5	0.157	4	103	76	7	0.8	176	3.5
46	3.56	0.5	8.8	8.5	0.157	2	102	110	16	0.9	175	2.8
47	4.07	0.48	8.3	9.1	0.157	4	90	90	25	0.9	plane	plane
48	4.37	0.45	8.3	8.5	0.157	6	89	81	9	0.9		
49	4.23	0.24	7.8	8.5	0.157	10	70	40	17	1.8	plane	plane
50	3.38	0.25	12.2	8.5	0.157	12	71	81	18	1	plane	plane
51	3.73	0.2	13.5	8.5	0.157	4	66	69	7	0.8	aliased	aliased
52	4.46	0.39	3.5	8.5	0.157	32	77	16	11	1.4	aliased	aliased
53	3.76	0.51	4.7	8.5	0.157	32	109	48	14	0.4	plane	plane
54	3.77	0.63	4.4	14.2	0.157	48	112	52	10	0.6	aliased	aliased
55	4.83	1.01	5.2	8.5	0.157	46	117	91				
56	4.43	0.95	6	14.2	0.157	42	135	111				
57	3.73	0.9	6.1	8.5	0.157	44	133	122	plane	plane	101	1.2
58	4.19	1	6.6	8.5	0.157	36	114	139	plane	plane	102	1.5
59	4.6	0.44	10.2	8.5	0.157	22	102	99	9	1	114	3.6
60	4.37	0.51	11.6	16.0	0.157	22	114	137	9	1	147	3.6
61	4.23	0.38	16	14.2	0.157	12	113	147	7	0.6	aliased	aliased
62	4.58	0.59	11.6	11.6	0.157	16	153	151	plane	plane	154	1.4
63	3.83	0.6	11.1	10.7	0.157	16	191	161	plane	plane	127	1.6
64	3.67	0.73	11.1	10.7	0.157	20	192	205	plane	plane	103	1.2
65	3.97	0.5	9.1	9.8	0.157	22	123	109	plane	plane		
66	4.56	0.38	9.5	9.1	0.157	16	115	78	plane	plane	93	1.8
67	4.05	0.46	9.8	9.1	0.157	12	130	106	plane	plane	123	1.8
68	3.71	0.42	10.7	9.8	0.157	18	144	110	plane	plane	132	1.8
69	3.94	0.69	9.5	9.1	0.157	20	113	156	plane	plane	164	2.3

Table 6. (continued)

Run	Depth, m	H_{m0}, m	T_{peak}, Sea Surface, s	T_{peak} Seabed, s	D_{50}, mm	Orbital Dir., deg	Sign. Orb. Dia., cm	Orbital Dia., cm	SWR Length, cm	SWR Height, cm	LWR Length, cm	LWR Height, cm
70	4.54	0.71	3.8	9.1	0.157	20	108	35	plane	plane	164	2.4
71	4.33	0.69	3.8	9.1	0.157	20	106	37	plane	plane	96	1.5
72	3.92	0.67	8.8	8.5	0.157	16	127	140	plane	plane	43	1.1
73	4.6	0.72	8	9.1	0.157	14	190	120	plane	plane	163	2.2
74	3.92	0.98	7.8	11.6	0.157	16	221	174	plane	plane	160	1.8
75	3.71	0.72	13.5	12.8	0.157	20	231	249				
76	4.06	0.95	12.2	12.8	0.157	20	242	278	plane	plane		
77	4.59	0.71	15.1	12.8	0.157	20	224	247	plane	plane		
78	4.06	0.83	12.8	11.6	0.157	20	239	252	plane	plane		
79	3.86	0.94	3.7	11.6	0.157	30	211	53				
80	4.44	1.27	12.2	12.8	0.157	28	198	349	plane	plane		
81	4.54	1.18	5.4	9.8	0.157	34	202	119				
82	4.06	1.14	9.8	10.7	0.157	20	257	264				
83	4.15	1.1	10.2	10.7	0.157	18	224	261				
84	4.67	0.92	11.6	12.8	0.157	22	218	235				
85	4.27	0.97	10.7	10.7	0.157	20	190	239				
86	4.91	0.84	4.7	12.8	0.157	44	130	61	plane	plane	153	2.5
87	4.07	0.81	4.7	12.8	0.157	36	146	71	plane	plane	134	2
88	3.96	1.13	4.7	10.7	0.157	32	152	102	plane	plane	108	1.4
89	4.94	1.06	5.3	9.1	0.157	36	153	97	plane	plane	89	2
90	4.03	1.34	10.2	11.6	0.157	28	271	321	plane	plane	140	1.6
91	4.38	1.12	10.7	10.7	0.157	24	374	270	plane	plane		
92	4.61	2.03	8.8	9.8	0.157	26	282	385	plane	plane	67	1
93	5.17	1.81	10.2	11.6	0.157	22	302	381	plane	plane	76	1
94	4.76	2.11	11.6	12.8	0.157	22	285	532			146	1.4
95	3.7	1.31	10.7	10.7	0.157	16	290	349				
96	4.11	1.51	6.1	10.7	0.157	20	261	192	plane	plane	149	1.2
97	5.14	1.16	6.4	10.7	0.157	26	222	135	plane	plane		
98	5	1.55	10.7	9.1	0.157	36	367	344				
99	4.08	2.18	9.5	8.5	0.157	36	369	482				
100	4.19	2.2	8.5	8.0	0.157	28	312	420				
101	5.06	2.33	7.8	8.5	0.157	32	345	353				
102	5.4	2.5	7.6	17.1	0.157	30	767	357				
103	4.43	2.4	9.5	9.5	0.157	24	822	500				
104	5.11	2.69	10.4	10.7	0.157	32	729	584				
105	4.59	2.34	10.7	11.6	0.157	28	514	545	plane	plane	75	1.6
106	4.92	1.88	13.5	13.5	0.157	30	547	543	plane	plane		
107	4.04	2.13	13.1	14.2	0.157	32	588	682				
108	4.72	1.87	10.9	13.5	0.157	28	685	441	plane	plane	93	1.7
109	4.45	1.93	9.8	12.8	0.157	24	420	418	plane	plane	116	1.6
110	4.96	1.87	12.2	14.2	0.157	26	443	490	plane	plane	124	2.1
111	4.31	1.57	14.2	14.2	0.157	22	502	527	plane	plane	208	1.1
112	4.45	1.43	14.2	13.5	0.157	22	453	474	plane	plane	191	2
113	4.58	1	12.2	12.8	0.157	16	274	271	plane	plane	176	2.2
114	4.43	1.28	11.6	12.8	0.157	26	277	340	plane	plane	164	2.1
115	3.86	1.12	10.7	12.8	0.157	34	237	287	plane	plane	114	0.8
116	4.25	1.24	12.2	11.6	0.157	32	224	354	plane	plane	135	1.2
117	3.9	1.11	11.6	11.6	0.157	30	199	311	plane	plane	161	1.9
118	4.5	0.89	10.2	11.6	0.157	26	170	202	plane	plane	181	1.8
119	4.41	0.81	11.1	12.8	0.157	28	158	205	plane	plane	202	1.5
120	3.79	0.72	11.1	11.6	0.157	30	149	195	plane	plane	185	2.6
121	4.08	0.51	9.8	10.7	0.157	18	152	118	plane	plane	188	3.1
122	3.74	0.41	10.2	10.7	0.157	14	116	103	plane	plane	180	2.9
123	4.21	0.53	10.7	10.7	0.157	8	96	130	21	1.2	124	2
124	4.32	0.37	9.8	9.1	0.157	14	93	82	21	2.4	71	2.1
125	3.73	0.4	9.8	9.1	0.157	−6	97	97	13	1.2	plane	plane
126	3.78	0.89	4.7	9.1	0.157	−8	164	83	plane	plane	plane	plane
127	3.59	1.16	8.3	8.5	0.157	−4	214	234	plane	plane	114	1
128	4.17	0.75	6.7	8.5	0.157	2	162	109	plane	plane	104	0.6
129	4.25	0.73	7.5	7.5	0.157	2	175	118	plane	plane	125	1.5
130	3.76	0.9	6.6	7.5	0.157	18	146	134	plane	plane	160	2
131	4.18	1.06	4.4	8.5	0.157	18	138	81	plane	plane	63	2.8
132	4.15	1.14	5.1	14.2	0.157	24	157	112	plane	plane	84	9.9
133	4.4	1.15	6.9	7.1	0.157	18	178	166	plane	plane	86	4
134	3.79	1.08	8.5	7.1	0.157	8	183	221	plane	plane	65	0.8
135	3.91	0.84	9.8	8.5	0.157	6	192	196	plane	plane	61	0.9
136	3.88	0.79	8	9.1	0.157	8	179	146	plane	plane	175	2.1
137	4.28	0.7	8.8	9.1	0.157	18	172	137	plane	plane	160	2.1
138	3.83	1.4	4.9	8.5	0.157	44	166	138	plane	plane	91	3

Table 6. (continued)

Run	Depth, m	H_{m0}, m	T_{peak}, Sea Surface, s	T_{peak} Seabed, s	D_{50}, mm	Orbital Dir., deg	Sign. Orb. Dia., cm	Orbital Dia., cm	SWR Length, cm	SWR Height, cm	LWR Length, cm	LWR Height, cm
139	4.16	1.29	6	7.1	0.157	44	233	158				
140	3.92	1.15	8	7.1	0.157	42	184	212	plane	plane	136	1.9
141	4.51	0.95	7.1	7.5	0.157	36	135	139	plane	plane	143	3.6
142	4.19	0.66	6.2	16.0	0.157	30	142	85	plane	plane	135	2.4
143	3.54	0.48	6.7	14.2	0.157	20	115	76	plane	plane	207	2.9
144	4.27	0.4	13.5	14.2	0.157	12	123	129	7	0.6	236	2.2
145	4.28	0.37	9.8	14.2	0.157	8	120	83	7	1.2	aliased	aliased
146	3.57	0.39	12.8	14.2	0.157	14	123	129	7	0.6	aliased	aliased
147	4.35	0.46	13.5	14.2	0.157	14	112	144	7	0.6	aliased	aliased
148	4.03	0.34	13.8	17.1	0.157	8	133	117	7	0.5	231	1.6
149	4.55	0.77	5.8	17.1	0.157	−16	402	85	plane	plane	230	2.8
150	4.26	1.78	7.8	9.1	0.157	4	288	303	plane	plane	178	1.1
151	3.72	1.1	8.5	8.5	0.157	4	293	228	plane	plane	172	1.8
152	4.35	1.19	9.3	10.2	0.157	2	350	246	plane	plane	125	0.8
153	4.52	1	8	9.1	0.157	4	302	168	plane	plane	114	0.6
154	4.44	0.96	9.5	9.8	0.157	10	284	201	plane	plane		
155	4.62	0.61	7.5	12.8	0.157	10	139	95	plane	plane	140	1.4
156	3.85	0.6	10.7	12.8	0.157	12	144	154	plane	plane	205	0.8
157	4.39	0.61	9	17.1	0.157	16	221	120	plane	plane		
158	4.21	0.56	11.6	10.7	0.157	16	162	154	plane	plane	175	1.2
159	4.56	0.64	9.3	17.1	0.157	30	197	129	plane	plane		
160	4.78	0.97	5.8	17.1	0.157	30	177	103	plane	plane	94	4.5
161	4.71	1.66	6.1	9.1	0.157	18	357	193				
162	4.21	1.23	9.5	10.7	0.157	22	277	267	plane	plane		
163	4.28	0.85	10.2	9.1	0.157	26	193	199	plane	plane		
164	3.79	0.64	11.1	12.8	0.157	24	195	174	plane	plane		
165	3.73	0.76	10.2	10.7	0.157	30	139	190	plane	plane		

[a]Definitions are same as in Table 5. No entry indicates quality of raw MTA data was too poor to obtain ripple estimates.

ments of the seabed profiles during periods when large wave groups occur. We found that even during brief periods of high mobility numbers, short wave ripple heights tend to be reduced. The subsequent rebuilding of these ripples in nearly the same locations then occurs during periods of lower mobility numbers. *Dingler and Inman* [1976] suggested that a single wave with a mobility number of 240 could flatten a rippled bed. Our measurements indicate that peak mobility numbers greater than ~150 result in the reduction of SWR height.

Ripple reformation can occur within a minute after flatten-

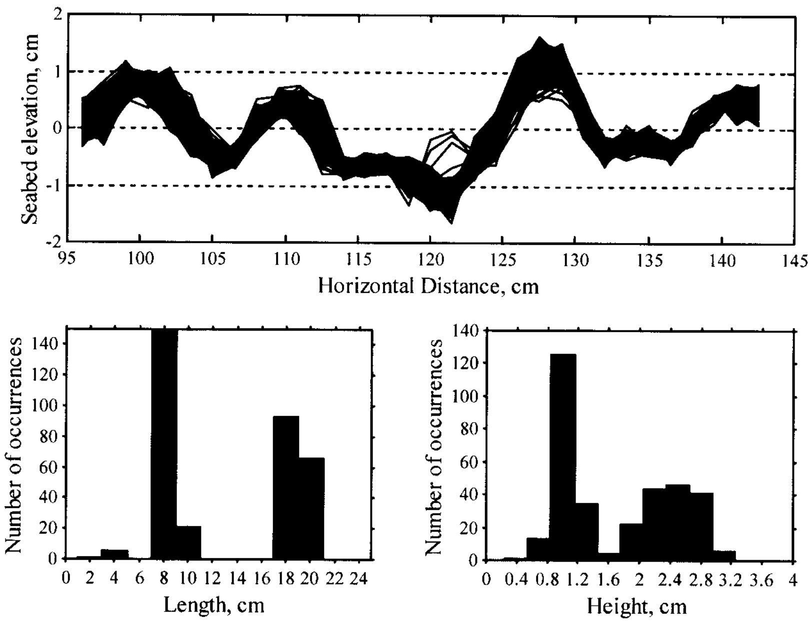

Figure 4. Example of SWR and their dimensions showing (top) representative detrended profiles for run 50 from the Sandyduck97 data set and (bottom) histogram distributions of ripple dimensions with number of occurrences.

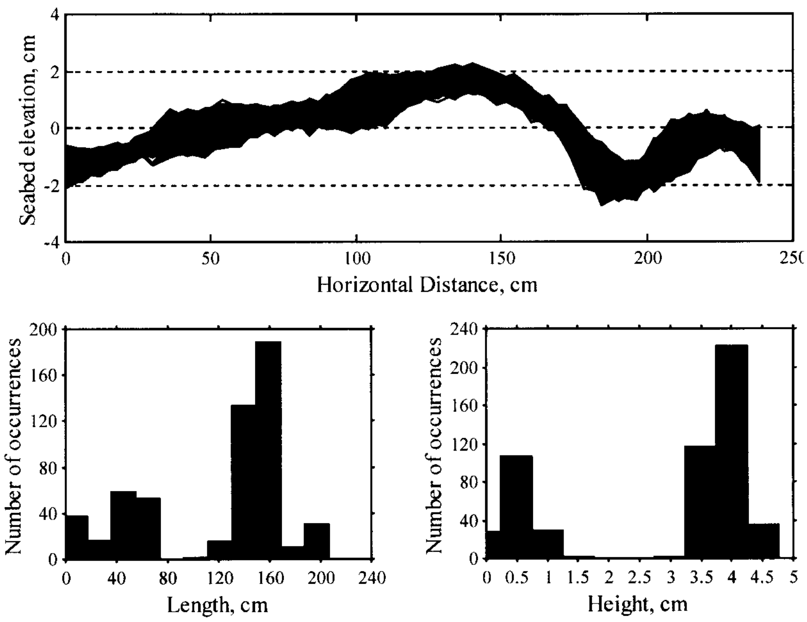

Figure 5. Example of LWR and their dimensions showing (top) representative detrended profiles for run 38 from the Sandyduck97 data set and (bottom) histogram distributions of ripple dimensions with number of occurrences.

ing and, in certain conditions, within a few wave periods. Once the peak mobility numbers decrease to values below ~150, the ripples tend to reform. If the peak mobility numbers are too low, the ripples will not reform until appropriate mobility numbers are reached. For most of our observations, when the peak mobility number remains below ~50, ripple reformation is slow or nonexistent. Once mobility numbers of >50 and <150 are reached and maintained, the ripples appear to reform rapidly, often within 1 min. Most of our observations of ripple reformation after flattening by wave groups indicate that the new ripple crests are coincident with the old. We suggest this is an indication that the seabed was not completely flattened but that undetectable SWR were still present.

Run 16 of the SIS96 experiment provides an example of SWR flattening and reformation, as shown in Figure 11. These observations were made in a water depth of 2.5 m with a significant wave height of ~0.6 m and a peak wave period of 10.7 s. The median sediment diameter was 0.21 mm. In Figure 11 the time series of ripple height was determined at each time step from the spatial standard deviation of the linearly detrended ripple profiles. The ripple height was calculated by multiplying the standard deviation by 2.83, which is the multi-

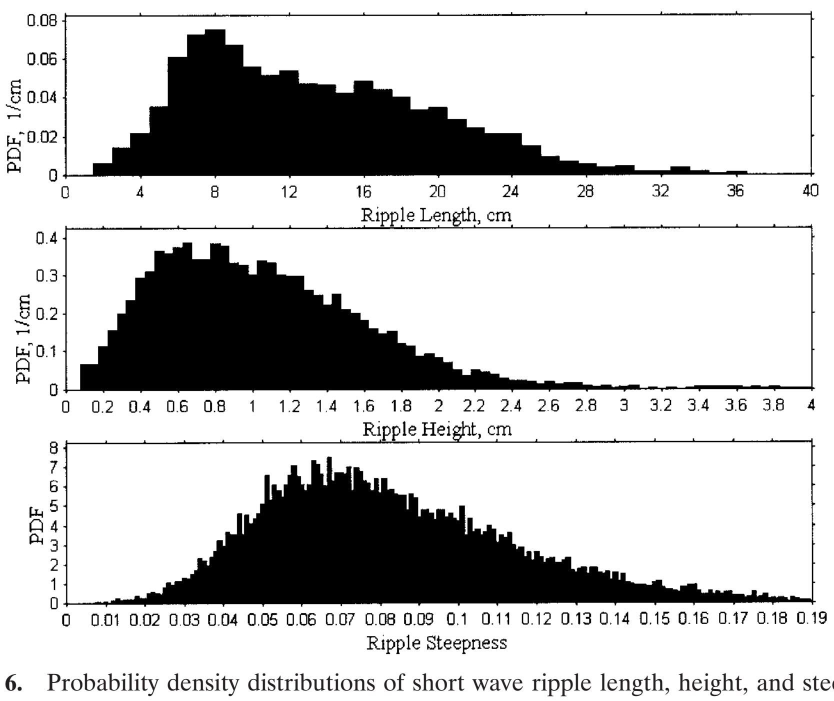

Figure 6. Probability density distributions of short wave ripple length, height, and steepness.

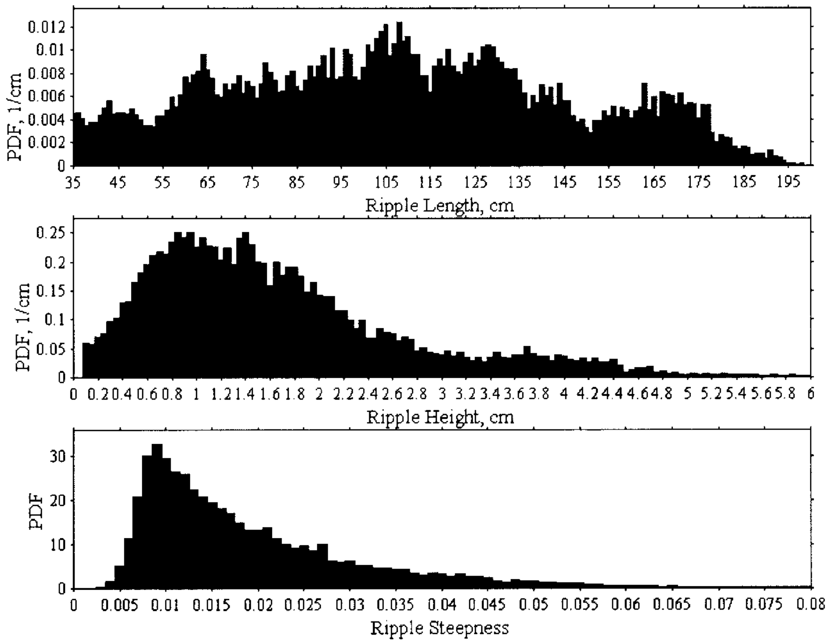

Figure 7. Probability density distributions of long wave ripple length, height, and steepness.

plier used to obtain height from standard deviation for sinusoidal curves. This multiplier is chosen simply to make the data presentation similar in magnitude to ripple height based upon trough to crest measurements. Figure 11a shows the time series of instantaneous near-bed mobility number defined as

$$|\Psi(t)| = \frac{[u(t)]^2}{(S-1)gD}.$$

In the middle of this run a large wave group with instantaneous peak-to-peak mobility numbers exceeding 200 resulted in the rapid flattening of the short wave ripple height. Following the flattening period, the ripple height began to increase. The crests appeared during the reformation period at approximately the same location they occupied just prior to the flattening, as shown in Figure 12 (described in section 6).

6. Ripple Migration

The migration of ripples can be estimated from time series of the seabed profiles measured by the MTA. Here we provide some examples of short and long wave ripple migration. These

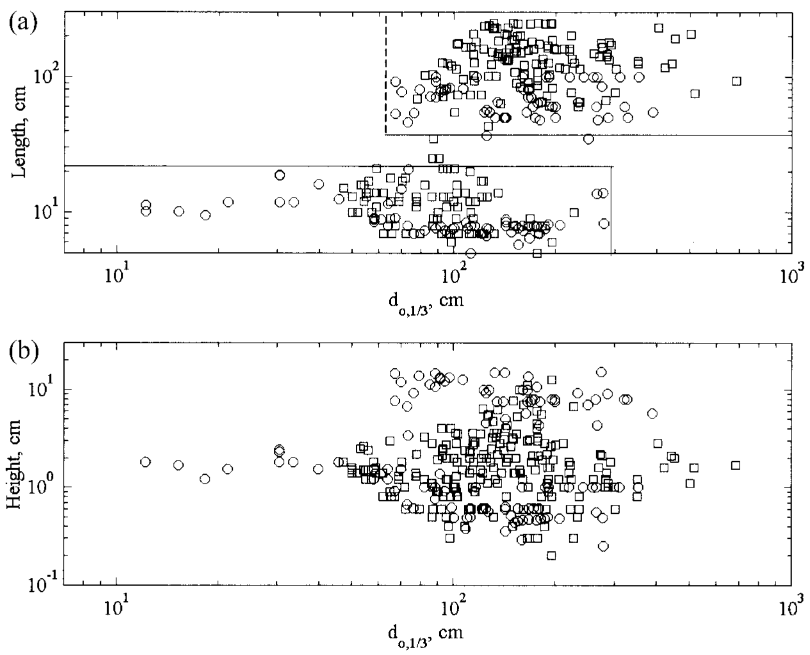

Figure 8. (a) Ripple length versus significant near bed orbital diameter. (b) Ripple height versus significant near-bed orbital diameter. Previous data are denoted by circles and present observations are denoted by squares.

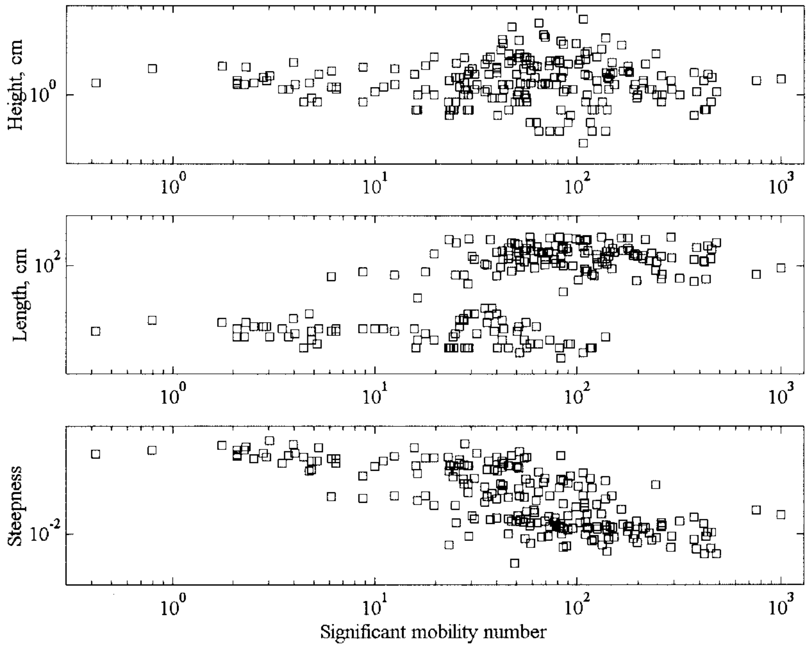

Figure 9. Ripple dimensions from SIS95, SIS96, and Sandyduck97 as a function of the significant near bed mobility number.

particular observations were made during the SIS96 experiment. Similar analysis of the Sandyduck97 data and a general explanation or model of the evolution and migration of ripples remain as future work.

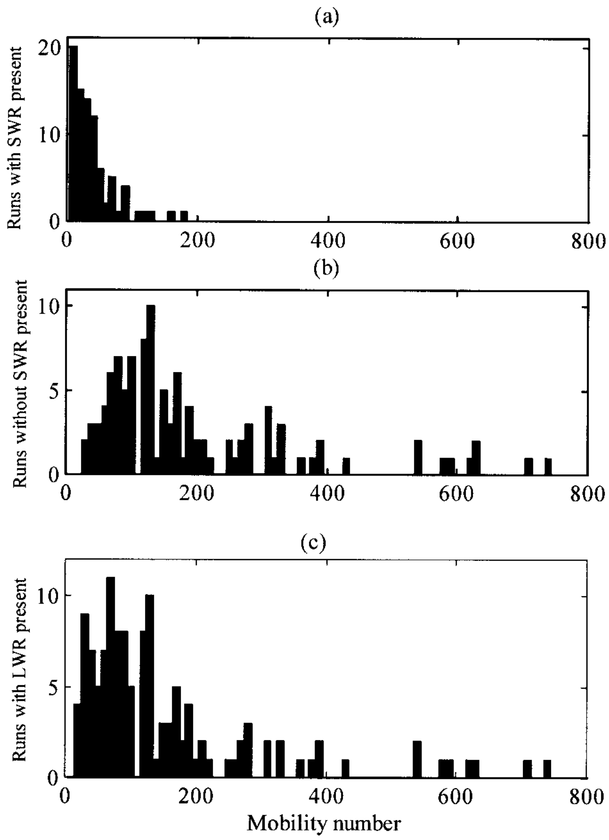

Figure 10. Number of runs in which (a) SWR were present, (b) SWR were not present, and (c) LWR were present.

During several of the observation periods, SWR were observed to migrate shoreward. Figure 12 is a depiction of the two-dimensional bed form profiles over time for run 16, described in section 5. Time is plotted on the y axis, with horizontal distance and elevation plotted on the x and z axis. The ripple crests are the light areas, and the troughs are the dark areas. Elevations are defined by the gray scale bar to the right of the plot in centimeters. The ripples migrated onshore an average of 6 cm during the first 8 min. This corresponds to an average onshore migration rate of 0.75 cm min^{-1}. The ripple dimensions during this period were also determined using the methods described in section 2 that estimate the extrema and zero crossings. These estimation techniques indicated that the ripples present during this period had average heights of 0.6 cm and lengths of 9 cm.

LWR were also sometimes observed to migrate. As with the SWR, the direction of migration was nearly always shoreward. For example, runs 19, 20, and 21 of the SIS96 data set documented the motion of a LWR over an 85-min period, as shown in Figure 13. Run 19, shown by the lowest group of curves, spans minutes 0–16. Run 20 is shown by the center group of curves and spans minutes 50–66. Run 21 is shown by the top group of curves and spans minutes 69–85. During these runs the ripple crest in the center of the profiles migrated ~50 cm. This corresponds to an average migration rate of 0.59 cm min^{-1}. The height of this bed form ranged from 4 to 6 cm, and the length ranged from 100 to 130 cm during the course of these runs.

Between runs 19 and 20, there was a gap of 34 min. During this period the waves increased in size and the ripple crest migrated shoreward to a greater degree than the ripple trough, resulting in elongation of the ripple. During run 20 the wave energy was higher than during run 19 or 21, with the highest values of the mobility number amplitude exceeding 200. The rate of migration during run 20 was about double the rate of migration during runs 19 and 21.

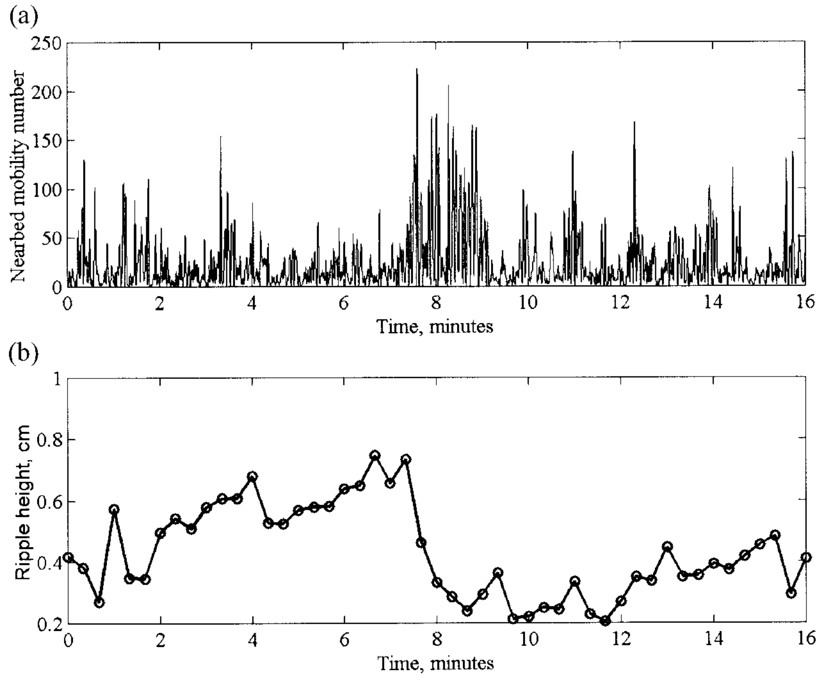

Figure 11. Time series of (a) mobility number and (b) ripple height for run 16 of the SIS96 experiment.

7. Model Comparison

Wave-formed ripple classification schemes and predictive models have emphasized the causative factors that determine horizontal and vertical length scales of the ripples. For example, *Clifton* [1976] identified orbital ripples that have wavelengths similar to the fluid orbital diameter and anorbital ripples that have wavelengths ~500 times the sediment grain diameter. He further suggested that the transition from orbital to anorbital is controlled by a critical value of the ratio of fluid orbital diameter to grain size. *Wiberg and Harris* [1994] used the same classification scheme in developing a predictive model for ripple geometry. They attribute the transition from orbital to anorbital ripples to the submersion of the ripple crest below the top of the wave boundary layer. It is interesting that in the orbital/anorbital classification paradigm, there exists a particular fluid orbital diameter that results in ripples with a maximum horizontal length scale for a fixed grain size, with shorter ripples at both smaller and larger fluid orbital diameters.

Here we compare the empirical ripple prediction models of *Nielsen* [1981] and *Wiberg and Harris* [1994] to previous field measurements [*Inman*, 1957; *Dingler*, 1974; *Nielsen*, 1981], and to our SIS95, SIS96, and Sandyduck97 data sets. The *Nielsen* [1981] model for irregular waves predicts the ripple height η and length λ of ripples using the near-bed semiexcursion A and the mobility number ψ. Nondimensional ripple height is expressed as

$$\eta/A = 21\psi^{-1.85} \qquad \psi > 10$$

$$\eta/A = 0.275 - 0.022\psi^{0.5} \qquad \psi < 10,$$

and nondimensional ripple length is expressed as

$$\frac{\lambda}{A} = \exp\left(\frac{693 - 0.37\ln^8\psi}{1000 + 0.75\ln^7\psi}\right).$$

Nielsen [1981] independently fit curves for ripple steepness, giving

$$\eta/\lambda = 0.342 - 0.34\sqrt[4]{\theta_{2.5}}.$$

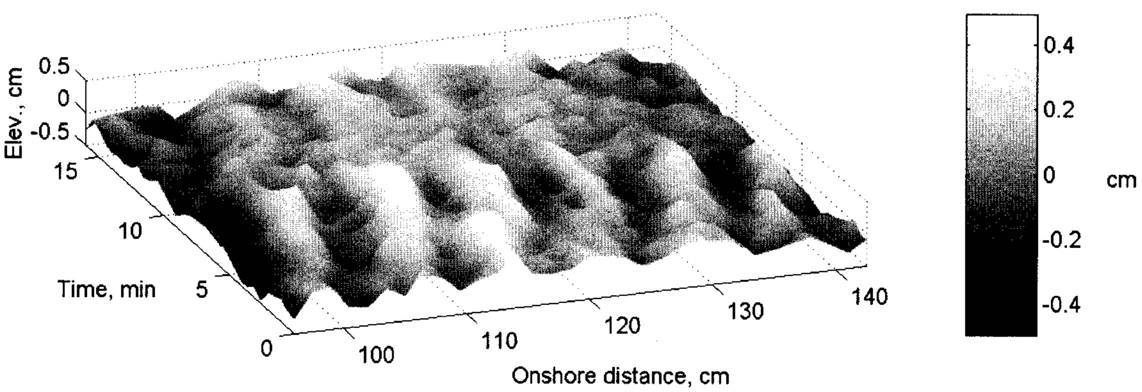

Figure 12. Bed form profiles for SWR (run 16 of the SIS96 experiment).

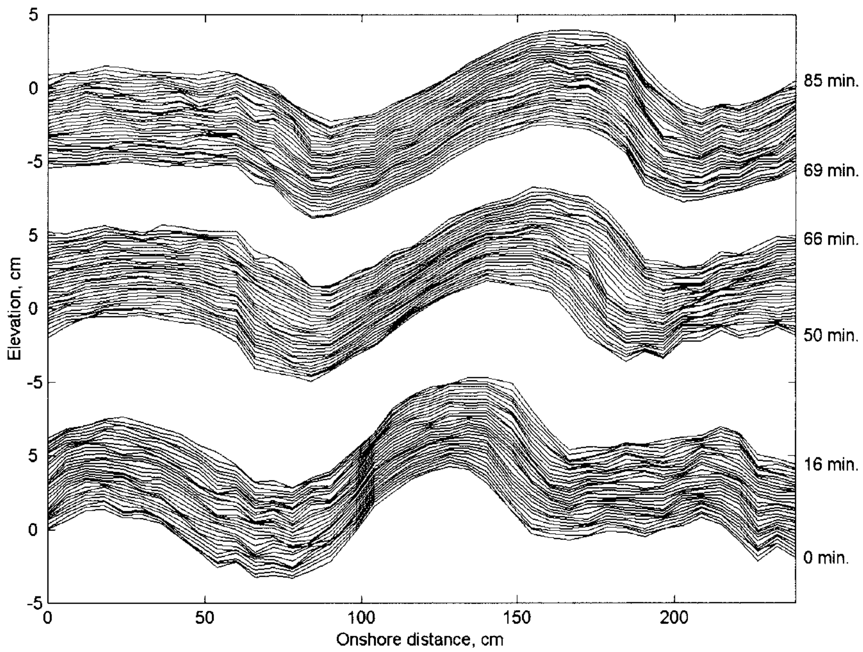

Figure 13. Bed form profiles for runs 19, 20, and 21 from the SIS96 experiment. There is a 1-min separation between profiles, and each profile is offset by +2 mm. Profile times are recorded on the right vertical axis.

The Shields parameter $\theta_{2.5}$ is defined by $\theta_{2.5} = \frac{1}{2} f_{2.5}\psi$, where $f_{2.5}$ is the *Swart* [1974] friction factor with a roughness of $2.5d_{50}$,

$$f_{2.5} = \exp\,[5.213(2.5d_{50}/A)^{0.194} - 5.977].$$

Wiberg and Harris [1994] classified bed forms according to the ratio of the near-bed orbital diameter ($d_o = 2A$) and anorbital ripple height (d_o/η_{ano}). This ratio is an approximation of the ratio of wave boundary layer thickness ($\delta_d \approx 0.04d_o$) to ripple height. Following *Clifton* [1976], ripples were classified as orbital, anorbital, or suborbital by the criteria given in Table 7. *Wiberg and Harris* [1994] found that orbital ripple length and height can be reasonably represented as a ratio of the near-bed orbital diameter

$$\lambda_{\mathrm{orb}} = 0.62d_o,$$

and that orbital ripple steepness remains roughly constant at

$$(\eta/\lambda)_{\mathrm{orb}} = 0.17.$$

From these two equations, orbital ripple height can be found directly as the product of orbital ripple length and steepness.

Wiberg and Harris [1994] suggested that anorbital ripple length is a function of grain size D only, giving

$$\lambda_{\mathrm{ano}} = 535D.$$

Previous studies such as those by *Nielsen* [1981] and *Grant and Madsen* [1982] had found ripple steepness to be a function of nondimensional bed shear stress; however, *Wiberg and Harris* [1994] found that anorbital ripple steepness can be defined in terms of (d_o/η). This allows the calculation of anorbital ripple height without the calculation of bed shear stress, which eliminates some of the complications and uncertainties involved in the computation of bed shear stress. *Wiberg and Harris* [1994] also found that ripple steepness (η/λ) in the nonorbital regimes (for $d_o/\eta > 10$) can be expressed as a function of the nondimensional orbital diameter (d_o/η) as

$$\eta/\lambda = \exp\,\{-0.095[\ln\,(d/\eta)]^2 + 0.442\,\ln\,(d_o/\eta) - 2.28\}.$$

Wiberg and Harris [1994] assumed that orbital ripple lengths are a function of orbital diameter and that anorbital ripple lengths are a function of grain diameter. By definition, suborbital ripples have ripple lengths that fall between these two limits. Thus a weighted geometric average of the bounding values of λ_{ano} and λ_{orb} was used to determine suborbital ripple length (λ_{sub}):

$$\lambda_{\mathrm{sub}} = \exp\,\{[(\ln\,(d_o/\eta_{\mathrm{ano}}) - \ln 100)/(\ln 20 - \ln 100)]$$
$$\cdot\,(\ln \lambda_{\mathrm{orb}} - \ln \lambda_{\mathrm{orb}}) + \ln \lambda_{\mathrm{orb}}\}.$$

The *Nielsen* [1981] model curves for ripple height, length, and steepness are shown in Figure 14 along with measured ripple dimensions. The *Nielsen* [1981] model captures the trends for the SWR but not for the LWR. This is shown more clearly in Figure 15, where only the SWR have been plotted.

The *Wiberg and Harris* [1994] ripple model curves are compared with measurements in Figure 16. In Figure 16a, ripple length data are compared to both the orbital and anorbital model curves. Similar to the *Nielsen* [1981] model, the Wiberg and Harris model captures the trends for the SWR but not for the LWR. Figure 17 shows the predictions of the Wiberg and Harris model for just the SWR observations.

A measure of the relative error Δ between measured and predicted values can be defined as

Table 7. *Wiberg and Harris* [1994] Ripple Classification

Flow Conditions	Ripple Classification
$d_o/\eta_{\mathrm{ano}} < 20$	orbital ripples
$20 < d_o/\eta_{\mathrm{ano}} < 100$	suborbital ripples
$d_o/\eta_{\mathrm{ano}} > 100$	anorbital ripples

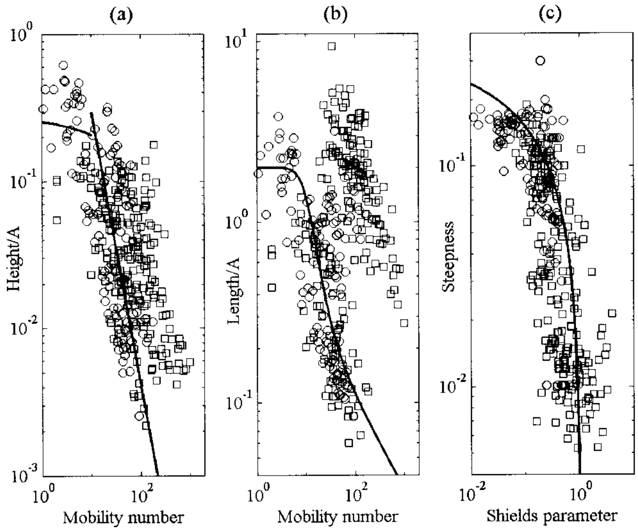

Figure 14. Dimensionless wave ripple (a) height and (b) length versus mobility number and (c) ripple steepness versus Shields parameter. Circles denote previous data, squares denote present data, and lines denote the *Nielsen* [1981] model curves.

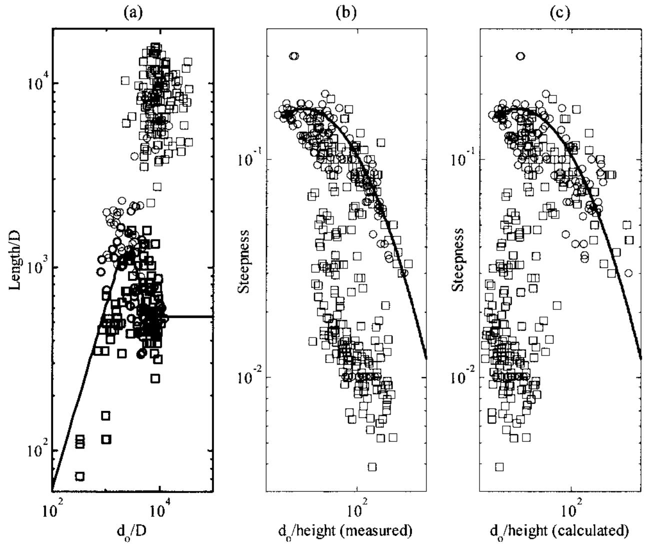

Figure 16. (a) Dimensionless ripple length versus dimensionless orbital diameter, (b) steepness versus orbital diameter/ripple height using the measured ripple height, and (c) steepness versus orbital diameter/ripple height using the predicted ripple height. Lines denote the predictions of *Wiberg and Harris* [1994].

$$\Delta = \exp\left\{\left[\left[(1/n)\sum_{1}^{n}(\ln(y)-\ln(\hat{y}))^2\right]^{1/2}\right]\right\}.$$

where $\hat{y}$ is the measured value and y is the predicted value. This quantity is a multiplicative factor that indicates the possible variation about the predicted value. For example, if Δ equals 1.34, the average error is equal to 34%.

The *Wiberg and Harris* [1994] ripple model and the *Nielsen* [1981] irregular wave ripple model performed similarly for the prediction of SWR dimensions. As shown in Table 8, the relative error for ripple height is 2.04 and 2.39 for the *Wiberg and Harris* [1994] and *Nielsen* [1981] ripple models, respectively. The models performed similarly at predicting ripple length and had relative errors of 1.81 and 1.93 for the *Wiberg and Harris* [1994] and *Nielsen* [1981] models, respectively. The models were better at predicting ripple steepness than at predicting ripple height or ripple length independently. The *Wiberg and Harris* [1994] ripple model had a relative error of 1.52, whereas the *Nielsen* [1981] model had a relative error of 1.59 in predicting ripple steepness.

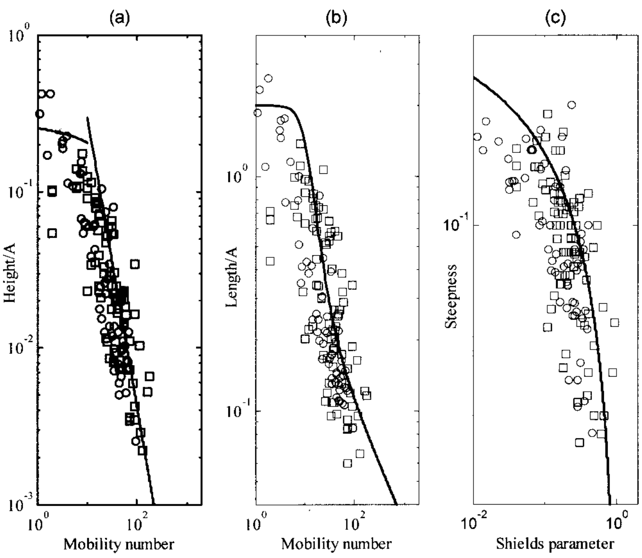

Figure 15. Dimensionless short wave ripple (a) height and (b) length versus mobility number and (c) ripple steepness versus Shields parameter. Circles denote previous data, squares denote present data, and lines denote the *Nielsen* [1981] model curves.

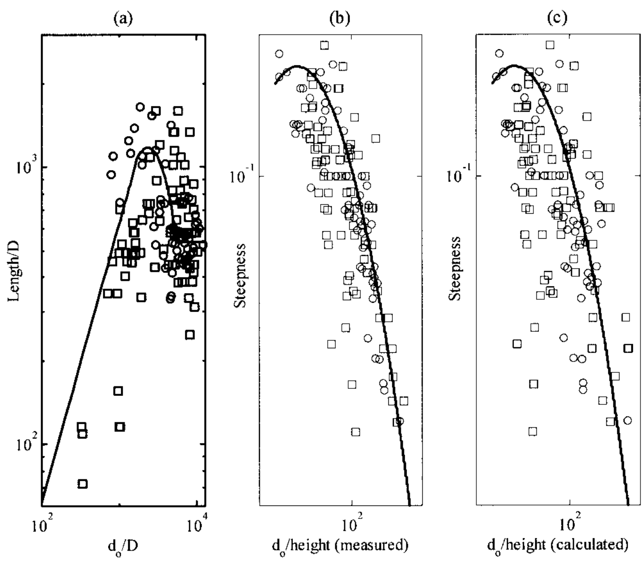

Figure 17. Same as Figure 16 but showing only SWR measurements.

Table 8. Relative Error Between Measured and Predicted SWR Dimensions

	Nielsen [1981] Measured	*Wiberg and Harris* [1994] Predicted
Ripple height	2.39	2.04
Ripple length	1.93	1.81
Ripple steepness	1.59	1.52

8. LWR Origins

The models were grossly inadequate in predicting the dimensions of the LWR, although it should be noted that their lengths are within approximately a factor of 2 of the near-bed significant orbital diameter, so there is at least the suggestion that they are orbital ripples. In order to examine the possible causes for existence of the LWR we attempted to find any correlation between the LWR dimension (mostly observed at the Sandyduck97 experiment) and different hydrodynamic parameters observed during the experiment, such as wave height, wave period, peak period of wave motion at the bottom, wave direction, water depth, mean velocities, and near-bed orbital diameter. At the level of significance $\alpha = 0.01$ the critical correlation coefficient for the LWR data was calculated to be 0.24. The highest correlation achieved between the LWR length and the hydrodynamic parameters was found to be 0.14, which cannot be considered as significant. The highest correlation for the LWR height was achieved with the peak period of wave motion at the bottom and was 0.34. One possible explanation for the low correlation between LWR dimensions and concurrent hydrodynamic forcing is that the LWR remain intact long after the hydrodynamic conditions have changed and are mainly relic features.

Even if LWR are orbital ripples, they are still particularly perplexing because of their low slopes. *Osborne and Vincent* [1993], *Gallagher et al.* [1998], *Thornton et al.* [1998], and others have reported bed forms with similar lengths, but the heights and slopes that we observed were lower than most previous observations. This could simply result from the relatively better ability of the MTA to measure low bed form heights. However, it raises issues related to the mechanisms of ripple formation. For example, if the ripple forms because of the shear stress distribution that results from flow separation, as is the generally accepted explanation, one must wonder if the flow truly separates, given the low observed slopes. Unfortunately, our observations are not sufficient to answer this question definitively. However, we have conducted a numerical simulation of the boundary layer using the measured bed form shapes and using wave forcing representative of the wave conditions.

The numerical simulation is called Dune 2D and is described by *Tjerry* [1995] and *Andersen* [1999]. The conditions for this simulation were observed on October 25, 1997. The LWR height and length were ~6 and ~90 cm, respectively, the water depth was 3.9 m, the significant wave height was 1.1 m, and the peak wave period was 8 s. The results of this simulation are shown in Figure 18. Figures 18a and 18c show the fluid velocity vectors at the time of the offshore to onshore flow reversal at various elevations above the seabed. Figures 18b and 18d show the turbulent kinetic energy distribution at the time of flow reversal. Figures 18a and 18b show results when the seabed consists of a LWR, and Figures 18c and 18d show results when the seabed consists of superimposed SWR (with length 7 cm and height 0.5 cm) and LWR. At the time of flow reversal shown in Figure 18 the flow far from the bed is still weakly offshore, but the flow near the bed has already reversed direction. Examination of the flow vectors in the LWR trough indicates that at the time of flow reversal, there is a small amount of flow separation and turbulence generation related to the LWR. Interestingly, if we perform the same simulation using a seabed consisting of superimposed SWR and LWR, as shown in Figures 18c and 18d, the amount of flow separation and turbulence is significantly increased. We therefore speculate that the LWR are essentially low-relief orbital ripples. We further speculate that the two scales of bed forms are not

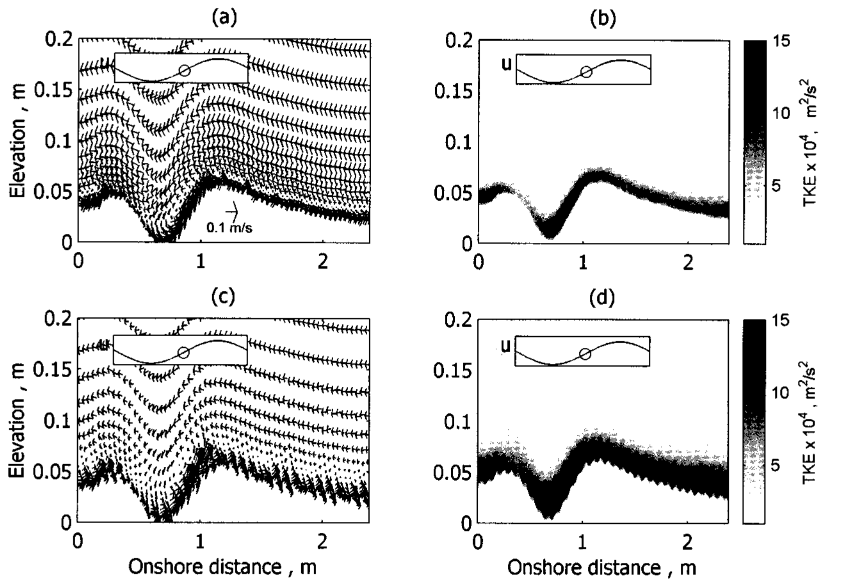

Figure 18. Results of Dune 2D simulation showing LWR seabed (a) fluid velocity vectors and (b) turbulent kinetic energy distribution at the time of offshore to onshore flow reversal and showing superimposed SWR and LWR seabed (c) fluid velocity vectors and (d) turbulent kinetic energy distribution at the time of flow reversal.

independent of each other and probably interact in a nonlinear fashion through the generation of turbulence and the separation of the flow.

9. Conclusions

A multiple transducer array was utilized to measure small-scale bed forms in the nearshore and inner shelf regions at Duck, North Carolina. The MTA measures the distance to the seabed with a vertical accuracy of ~3 mm at a series of transducers arranged on a linear transect. The data can then be interpreted to estimate the dimensions of wave-formed ripples on the seabed. Three intense periods of observation were carried out to measure the small-scale bed forms and accompanying hydrodynamics.

Two populations of wave-formed ripples were observed: short wave ripples (SWR) with heights ranging from 3 mm to 2 cm and lengths ranging from 4 to 25 cm and long wave ripples (LWR) with heights ranging from 3 mm to 6 cm and lengths ranging from 35 to 200 cm. The SWR were only present sometimes, and their presence or absence was determined to some extent by a critical value of the near-bed mobility number. The SWR were highly dynamic, sometimes flattening during wave groups and reforming over several incident wave periods. The SWR were found to decrease in height in response to individual waves when the near-bed mobility number exceeded ~150. The LWR, in contrast, were almost always present. They were longer and had lower relief than was predicted by models or generally observed previously.

Both SWR and LWR were often observed to migrate shoreward but rarely observed to migrate seaward. The dimensions of the SWR, when they were present, were predictable by the *Nielsen* [1981] model or the *Wiberg and Harris* [1994] model to within approximately a factor of 2. A numerical simulation of the boundary layer indicates weak separation and turbulence production above the LWR, with significant enhancement of these processes when SWR are superimposed upon LWR.

Acknowledgments. We gratefully acknowledge the financial support of the Coastal Sciences Program of the U.S. Office of Naval Research and the National Ocean Partnership Program. We would also like to thank the staff of the USACOE Field Research Facility and the other numerous individuals who assisted with the field deployments. Thanks are also owed to Patricia Wiberg for providing a helpful review of this paper.

References

Andersen, K. H., The dynamics of ripples beneath surface waves and topics in shell models of turbulence, Ph.D. thesis, Tech. Univ. of Denmark, Copenhagen, 1999.
Bagnold, R. A., Motion of waves in shallow water: Interaction of waves and sand bottoms, *Proc. R. Soc. London*, *Ser. A*, *187*, 1–15, 1946.
Boyd, R., D. L. Forbes, and D. E. Heffler, Time-sequence observations of wave-formed sand ripples on an ocean shore face, *Sedimentology*, *35*, 449–464, 1988.
Carstens, M. R., R. M. Nielson, and H. D. Altinbilek, Bedforms generated in the laboratory under oscillatory flow: Analytical and experimental study, *Tech. Memo. 28*, U.S. Corps of Eng., Coastal Eng. Res. Cent., Fort Belvoir, Va., June 1969.
Clifton, H. E., Wave formed sedimentary structures: A conceptual model in beach and near-shore sedimentation, edited by R. A. Davis Jr. and R. L. Ethington, *Spec. Publ. SEPM*, *Soc. Sediment. Geol. 24*, 126–148, 1976.
Dingler, J. R., Wave formed ripples in near-shore sands, Ph.D. thesis, Univ. of Calif., San Diego, 1974.
Dingler, J. R., and D. L. Inman, Wave-formed ripples in near-shore sands, paper presented at 15th Conference of Coastal Engineers, Am. Soc. of Civ. Eng., Honolulu, Hawaii, 1976.
Dingler, J. R., J. C. Boylls, and R. L. Lowe, High-frequency sonar for profiling small-scale subaqueous bedforms, *Mar. Geol.*, *24*, 279–288, 1977.
Gallagher, E. L., S. Elgar, and E. B. Thornton, Megaripple migration in a natural surf zone, *Nature*, *394*(6689), 165–168, 1998.
Grant, W. D., and O. S. Madsen, Movable bed roughness in unsteady oscillatory flow, *J. Geophys. Res.*, *87*, 469–481, 1982.
Greenwood, B., R. G. Richards, and R. W. Brander, Acoustic imaging of seabed geometry—A high resolution remote tracking sonar (HR-RTS-II), *Mar. Geol.*, *112*, 207–218, 1993.
Hay, A. E., and D. J. Wilson, Rotary sidescan images of nearshore bedform evolution during a storm, *Mar. Geol.*, *119*, 57–65, 1994.
Inman, D. L., Wave generated ripples in near-shore sands, *Tech. Memo. 100*, 66 pp., U.S. Army Corps of Eng., Beach Erosion Board, Washington, D. C., 1957.
Jette, C. D., Wave-generated bedforms in the near-shore sand environment, Ph.D. dissertation, Univ. of Fla., Gainesville, 1997.
Jette, C. D., and D. M. Hanes, High-resolution sea-bed imaging: An acoustic multiple transducer array, *Meas. Sci. Technol.*, *8*, 787–792, 1998.
Li, M. Z., and C. L. Amos, Sheet flow and large wave ripples under combined waves and currents: Field observations, model predictions, and effects on boundary layer dynamics, *Cont. Shelf Res.*, *19*, 637–663, 1999.
Miller, M. C., and P. D. Komar, Oscillation sand ripples generated by laboratory apparatus, *J. Sediment. Petrol.*, *50*, 173–182, 1980a.
Miller, M. C., and P. D. Komar, A field investigation of the relationship between oscillation ripple spacing and the near-bottom water orbital motions, *J. Sediment. Petrol.*, *50*, 183–191, 1980b.
Mogridge, G. R., M. H. Davies, and D. H. Willis, Geometry prediction for wave-generated bedforms, *Coastal Eng.*, *22*, 255–286, 1994.
Nielsen, P., Dynamics and geometry of wave-generated ripples, *J. Geophys. Res.*, *86*, 6467–6472, 1981.
Nielsen, P., *Coastal Bottom Boundary Layers and Sediment Transport*, 324 pp., World Sci., River Edge, N. J., 1992.
Osborne, P. D., and C. E. Vincent, Dynamics of large and small scale bedforms on a macrotidal shoreface under shoaling and breaking waves, *Mar. Geol.*, *115*, 207–226, 1993.
Southard, J. B., J. M. Lambie, D. C. Federico, H. T. Pile, and C. R. Weidman, Experiments on bed configurations in fine sands under bidirectional purely oscillatory flow, and the origin of hummocky cross-stratification, *J. Sediment. Petrol.*, *60*, 1–17, 1990.
Swart, D. H., Offshore sediment transport and equilibrium beach profiles, *Lab. Publ. 131*, Delft Hydraul., Delft, Netherlands, 1974.
Thornton, E. B., J. L. Swayne, and J. R. Dingler, Small-scale morphology across the surf zone, *Mar. Geol.*, *145*, 173–196, 1998.
Tjerry, S., Morphological calculation of dunes in alluvial rivers, Ph.D. thesis, Tech. Univ. of Denmark, Copenhagen, 1995.
Traykovski, P., A. E. Hay, J. D. Irish, and J. F. Lynch, Geometry, migration, and evolution of wave orbital ripples at LEO-15, *J. Geophys. Res.*, *104*, 1505–1524, 1999.
Tunsdall, E. B., and D. L. Inman, Vortex generation by oscillatory flow over rippled surfaces, *J. Geophys. Res.*, *80*, 3475–3484, 1975.
Vincent, C. E., and P. D. Osborne, Bedform dimensions and migration rates under shoaling and breaking waves, *Cont. Shelf Res.*, *13*, 1267–1280, 1993.
Vincent, C. E., S. W. Marsh, M. P. Webb, and P. D. Osborne, Spatial and temporal structures of suspension and transport over megaripples on the shore face, *J. Geophys. Res.*, *104*, 11,215–11,224, 1999.
Wheatcroft, R. A., Temporal variation in bed configuration and one-dimensional bottom roughness at the mid-shelf STRESS site, *Cont. Shelf Res.*, *14*, 1167–1190, 1994.
Wiberg, P. L., and C. K. Harris, Ripple geometry in wave-dominated environments, *J. Geophys. Res.*, *99*, 775–789, 1994.

V. Alymov, Y. S. Chang, and D. M. Hanes, Department of Civil and Coastal Engineering, University of Florida, P.O. Box 116590, Gainesville, FL 32611-6590, USA. (alymov@ufl.edu; yschang@ufl.edu; hanes@ufl.edu)

C. Jette, Seatek Inc., 5108 NW 27th Drive, Gainesville, FL 32605, USA. (chris@seatek.com)

(Received March 29, 2000; revised June 4, 2001;
accepted June 4, 2001.)